Quasi-elastic and inelastic neutron scattering in the high temperature phase of the cooperative Jahn-Teller system $CsCuCl_3$

Quasi-elastic and inelastic neutron scattering in the high-temperature phase of the cooperative Jahn–Teller system CsCuCl₃

H A Graf†‡, G Shirane†, U Schotte§, H Dachs§, N Pyka§ and M Iizumi‖

† Brookhaven National Laboratory, Upton, NY 11973, USA
§ Hahn-Meitner-Institut, Glienicker Strasse 100, D-1000 Berlin 39, Federal Republic of Germany
‖ Japan Atomic Energy Research Institute, Tokai, Ibaraki 319-11, Japan

Abstract. Quasi-elastic and inelastic neutron measurements have been performed to study the high-temperature phase of the cooperative Jahn–Teller system CsCuCl₃. A strong coupling between phonons and dynamic reorientation processes of the distorted CuCl₆ octahedra has been detected. Applying a theoretical approach, which is based on phonon-mediated dipole–dipole interactions using the concept of pseudo-spins for describing the orientational disorder of the Jahn–Teller distorted octahedra, it is possible to interpret the characteristic features of the quasi-elastic and inelastic scattering in a unified picture. The relaxation rate of the reorientation processes was determined as 2×10^{10} s^{-1} and it is shown that the warping energy can be derived from a systematic measurement of the relaxation rate as a function of temperature.

1. Introduction

The phase transitions in hexagonal perovskites AMCl₃ with Jahn–Teller active ions M = Cu²⁺, Cr²⁺ and alkali ions A = Rb⁺, Cs⁺ have been studied extensively in the past (Hirotsu 1977, Crama 1980, Crama and Maaskant 1983, Tanaka *et al* 1986a, b). These compounds are characterised by isolated chains of face-sharing MCl₆ octahedra extending along the hexagonal *c* axis. They have a common high-temperature structure of space group P6₃/mmc, which corresponds to the CsNiCl₃ type according to x-ray diffraction experiments. The structure is shown schematically in figure 1. With decreasing temperature the Cs compounds undergo one phase transition and the Rb compounds two phase transitions.

The low-temperature structure of CsCuCl₃, as distinguished from the other compounds, remains hexagonal with space group P6₁22 and the *c* axis tripled, while the *a* axis is almost unaltered. The phase transition occurs at 423 K and is predominantly of first order. In accordance with the Jahn–Teller theorem, all CuCl₆ octahedra in this phase are found to be tetragonally elongated with the long axes being helically arranged in such a way that they do not meet at the same Cl atom of a Cl₃ face shared by

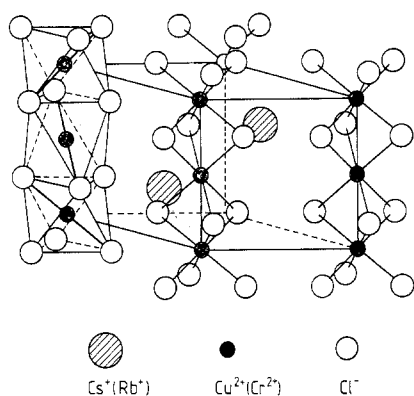‡ Work performed while on leave from Hahn-Meitner-Institut, to where this author has now returned.

Figure 1. The high-temperature structure of the hexagonal perovskites $AMCl_3$, with $A = Cs^+$, Rb^+ and $M = Cu^{2+}$, Cr^{2+}. The unit cell contains two formula units.

neighbouring octahedra. This 'exclusion principle' is also valid in the low-temperature structures of the related compounds, which are monoclinic with the c axis doubled.

Since the Jahn–Teller energy of Cu^{2+} ions in an octahedral environment is known to be very high (see e.g. Reinen and Friebel 1979), one has to assume that the $CuCl_6$ octahedra are also distorted in the high-temperature phase above T_c and that the apparent high symmetry $P6_3/mmc$ found in diffraction experiments is generated by averaging over static or dynamic disorder. Graf *et al* (1986) observed strong diffuse intensity around Bragg reflections with large structure factors, which was interpreted as 'dense impurity' scattering and described by the Huang formalism. The distorted octahedra are conceived as 'impurities' being embedded in the elastic matrix of the ideal $CsNiCl_3$ lattice. The long axes of the octahedra are supposed to be randomly oriented over six equivalent directions, thus giving rise to the apparent high symmetry.

The neutron experiments described by Graf *et al* (1986) were performed on a two-axis diffractometer. It was the objective of the present work to reinvestigate the diffuse scattering using a triple-axis spectrometer for separating off possible phonon contributions and to perform inelastic measurements on selected phonon branches to study the dynamic properties of the high-temperature phase. These experiments led to the discovery of a strong coupling between phonons and dynamic reorientation processes of the $CuCl_6$ octahedra. By introducing the concept of a pseudo-spin, it was possible to develop further the Huang theory sketched by Graf *et al* (1986) and elaborated by Schotte (1987) so as to include the dynamical properties of the system, using and extending a method described by Yamada *et al* (1974). With this advanced theory the quasi-elastic and inelastic scattering observed in the high-temperature phase of $CsCuCl_3$ can be described in a unified picture.

2. Experimental

2.1. General

Two samples were used in the present experiments. Sample A, on which most of the measurements were performed and which had already been used in former experiments, was a single crystal of about 1 cm^3 grown from aqueous solution. It turned out that
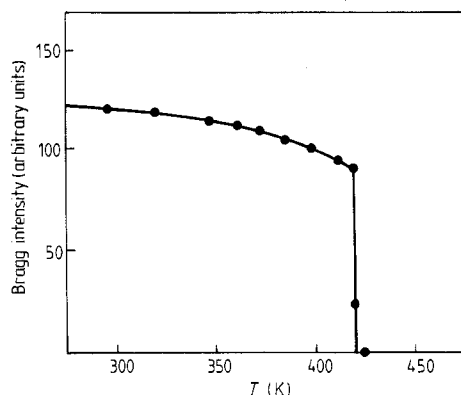
Figure 2. Bragg intensity of the superlattice reflection $(2,0,\frac{2}{3})$ as a function of temperature (the indices refer to the high-temperature unit cell). The measurements were performed on sample C. (In this and all subsequent figures, the phase transition temperature of the CsCuCl₃ crystals is $T_c = 423$ K.)

CsCuCl₃ single crystals rapidly degrade when being cycled through the phase transition. At the end of the experiments sample A showed weak powder lines and had a mosaic spread of 50 minutes of arc. For final experiments, therefore, a second crystal, newly grown from aqueous solution, was used. This crystal, sample B, had a volume of about 2 cm³ and a mosaic spread of 20 minutes of arc. Below, a former study of the temperature dependence of the superlattice reflections and the diffuse scattering is referred to, which was performed on a single crystal, sample C, of about 1 cm³ volume (Iizumi *et al* 1977).

The neutron measurements were carried out on triple-axis spectrometers of the high-flux beam reactor HFBR at Brookhaven National Laboratory. For all experiments the crystals, wrapped in aluminium foil, were mounted in a furnace with their $(h0l)$ zone in the scattering plane.

Pyrolytic graphite was used as monochromator and analyser. The quasi-elastic measurements were mainly made with 14.7 meV neutron radiation and horizontal collimation angles of $20'-20'-20'-20'$ (minutes of arc). The analyser was set for zero energy transfer of the scattered neutrons and a graphite filter was used to eliminate the higher-order contamination. Sample C was investigated under the same conditions, except that the energy of the incoming neutrons was 13.5 meV.

All inelastic measurements were performed in the constant-Q mode keeping the final energy fixed. Phonons with q-values larger than 0.15 Å⁻¹ were investigated using a final energy of 14.7 meV and horizontal collimations of $20'-20'-20'-20'$ and $40'-20'-40'-40'$. Phonons at smaller q-values were measured on a double-monochromator spectrometer located at the cold source of the HFBR. Here, the final energy was fixed at 5 and 3 meV, respectively, while the horizontal collimations were $60'-40'-60'-40'-40'$.

No effort was made to determine the phase transition temperature T_c and the lattice constants precisely. In any measurement close to T_c, however, the positions of the superlattice reflections were examined for Bragg intensity, in order to decide whether the crystal was above or below T_c. The intensity of the $(2,0,\frac{2}{3})$ reflection as a function of temperature is shown in figure 2 (all indices in the present paper refer to the high-temperature unit cell). This measurement made on sample C indicates that the phase transition is predominantly of first order. A value of 423 K was assigned to T_c.

Table 1. Lattice constants as a function of T and elastic constants from Soboleva *et al* (1976) for $CsCuCl_3$. The lattice constants and cell volumes listed refer to the high-temperature unit cell ($T_c = 150\,°C$). The last digits are uncertain. Values marked by an asterisk should be multiplied by 3 to conform with the low-temperature unit cell. The densities are calculated values.

T (°C)	a (Å)	c (Å)	V (Å^3)	ρ (g cm^{-3})
20	7.214	6.058*	273.0*	3.683
54	7.224	6.069*	274.3*	3.666
145	7.255	6.096*	277.9*	3.618
155	7.227	6.150	278.2	3.614
203	7.246	6.158	280.0	3.591
251	7.273	6.175	282.9	3.554

Elastic constants (10^{10} dyn cm^{-2})

$c_{11} = 28.96$	$c_{12} = 11.28$	$c_{13} = 10.30$
$c_{33} = 46.49$	$c_{44} = 5.49$	$c_{66} = (c_{11} - c_{12})/2$
		$= 8.84$

The lattice constants obtained at various temperatures are summarised in table 1 together with the calculated unit-cell volumes and densities. Since not more than three reflections were used for determining these constants, they should mainly be regarded as indicative for the trend. To make comparison easier, the values for $c/3$ and $V_{cell}/3$ are listed in the case of the low-temperature phase. The elastic constants of $CsCuCl_3$ determined by Soboleva *et al* (1976) at room temperature are also included in table 1.

2.2. Quasi-elastic measurements

Strong quasi-elastic diffuse scattering is found in $CsCuCl_3$ above T_c. It is centred at the Bragg points of the high-temperature phase and can be observed well in the vicinity of reflections with large structure factors, where it extends far out into the Brillouin zone. At T_c the diffuse scattering vanishes and the superlattice reflections of the low-temperature phase appear at positions corresponding to a tripling of the c axis.

Figure 3 shows scans performed along Q_x and Q_z (a^* and c^* directions) in the ($h0l$) plane of the reciprocal lattice at temperatures $T = T_c + 5$ K and $T = T_c - 5$ K, respectively. The scan geometry in reciprocal space is indicated in the insets. For these measurements all horizontal collimations were 20 minutes of arc and the analyser of the triple-axis spectrometer was set to reflect neutrons of zero energy transfer only. Above T_c, quasi-elastic diffuse scattering appears as broad tails of the strong Bragg reflections (201), (202) and (002). The relatively large width of the (002) reflection in the measurement below T_c is a consequence of the large mosaic spread and the weak (002) powder line present in sample A. No indication for critical scattering at the superlattice positions $(2,0,1 \pm \frac{1}{3})$ is observed. More detailed measurements of the scattering around $(2,0,\frac{2}{3})$ at temperatures less than 1 K above T_c failed to reveal any scattering peak at this point.

The extension of the diffuse scattering in the ($h0l$) plane around (201) and (002) is shown in figures 4(a) and 5(a). These iso-intensity contour plots are based on a mesh of intensities obtained by scanning parallel to Q_x and Q_z (examples for such scans are
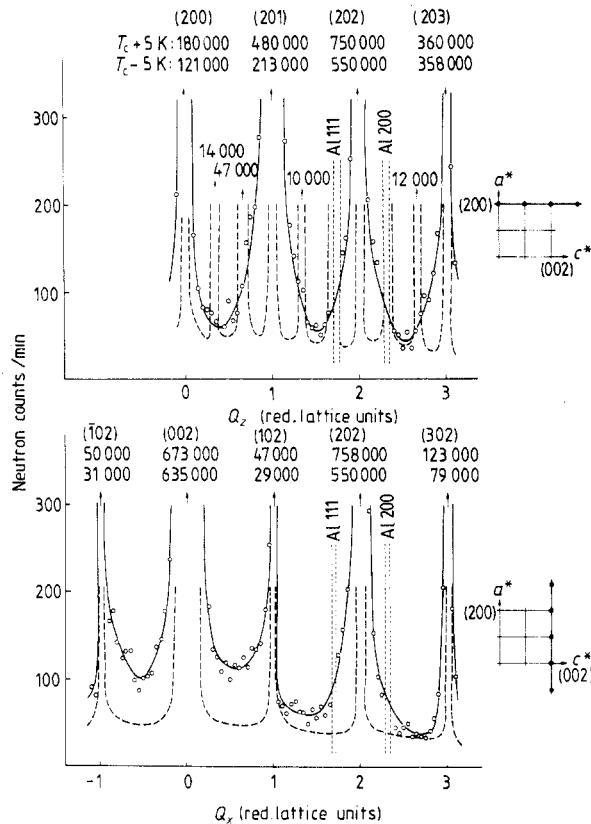
Figure 3. Scans along a^* (lower part) and c^* (upper part) measured on sample A at $T_c + 5\,K$ (open circles) and $T_c - 5\,K$ (broken curves), respectively. The full curves are guides to the eye. The tails of the 202 reflection are contaminated with aluminium lines. The scan direction is indicated in the sketches of the reciprocal lattice. Horizontal collimations, $20'-20'-20'-20'$; $E = 0\,\text{meV}$.

shown in figure 11). The iso-intensity contours demonstrate that the diffuse scattering around (002) is concentrated in lobes along Q_x only, while the scattering around (201) is extended in both directions, Q_x and Q_z, with smaller side lobes along Q_x and larger main lobes along Q_z. The background level in these measurements is about 40 counts min^{-1}. Directly along the lines $(q_x,0,1)$ and $(q_x,0,2)$, however, the intensity does not completely fall off to this level. The shaded ellipses centred at the Bragg points represent the instrumental resolution and the chain curves indicate weak powder lines visible in the scans, which stem from the strong Bragg reflections. The diffuse intensity pattern around (202) has lobes of approximately equal length in Q_x and Q_z directions. It was not measured in detail, since this region is contaminated with aluminium lines caused by the sample environment.

The diffuse scattering was analysed by determining the linewidth 2Γ of the individual scans deconvoluted with the instrumental resolution. The intrinsic lineshape of the measured profiles was assumed to be Lorentzian. The results are summarised in figure 6. Here, the (201) main lobe is characterised by plotting the linewidth 2Γ of scans performed parallel to Q_x at distances q_z from the Bragg point. For the (201) side lobe and the (002) lobe the linewidths 2Γ of scans parallel to Q_z at distances q_x are plotted.
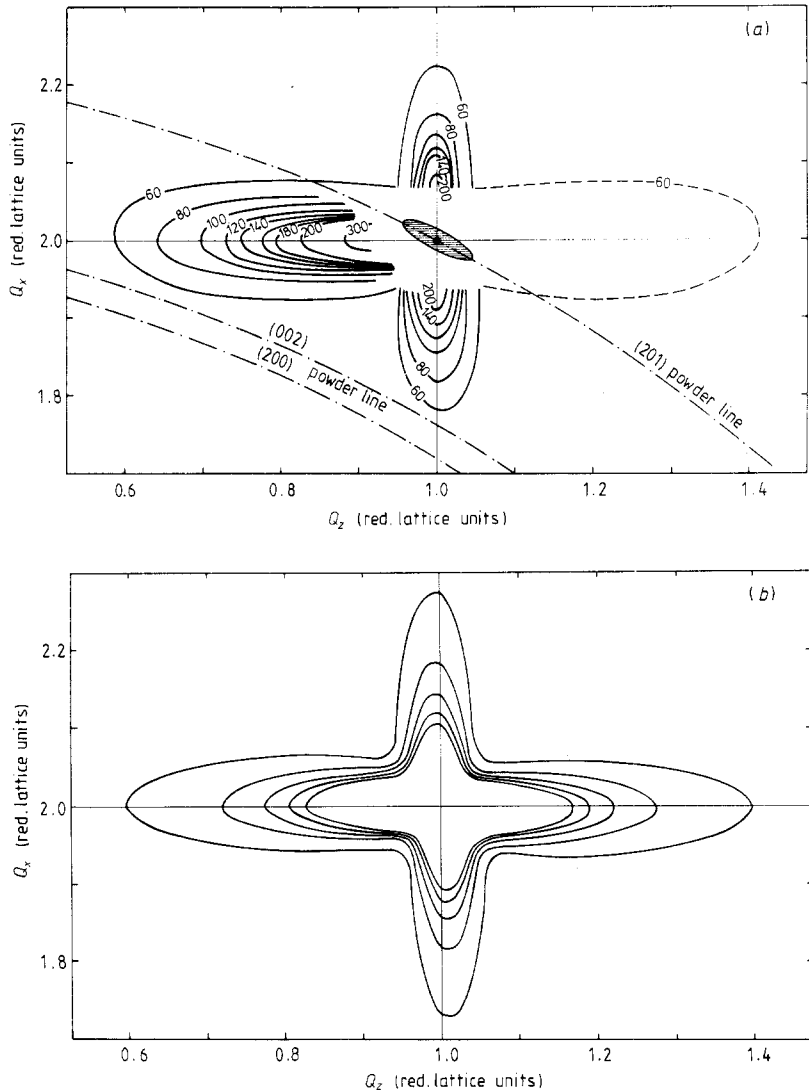
Figure 4. (*a*) Diffuse scattering around (201) measured at $T = T_c + 5$ K on sample A. The background level is about 40 counts min^{-1}. The instrumental resolution is indicated by the shaded ellipse centred at the Bragg point. The data are contaminated with powder lines indicated by the chain curves. The main lobe at the right-hand side has not been measured in detail. (*b*) Calculated iso-intensity contours around (201) at $T = T_c + 5$ K convoluted with the instrumental resolution for sample A. The lines represent equidistant intensity values in arbitrary units. For details of the calculation see text (§ 4.2). Horizontal collimations, $20'$–$20'$–$20'$–$20'$; $14.7E_f$; $E = 0$ meV.

Within the experimental errors, which are rather large for sample A, but small for sample B, the linewidth 2Γ is a linear function of q. As shown by Schotte (1987) such behaviour points to Huang-type scattering and the straight lines in figure 6 are theoretical predictions based on the 'extended Huang' theory presented in § 3. Qualitatively, the form of the diffuse patterns does not change with increasing temperature, only the intensity
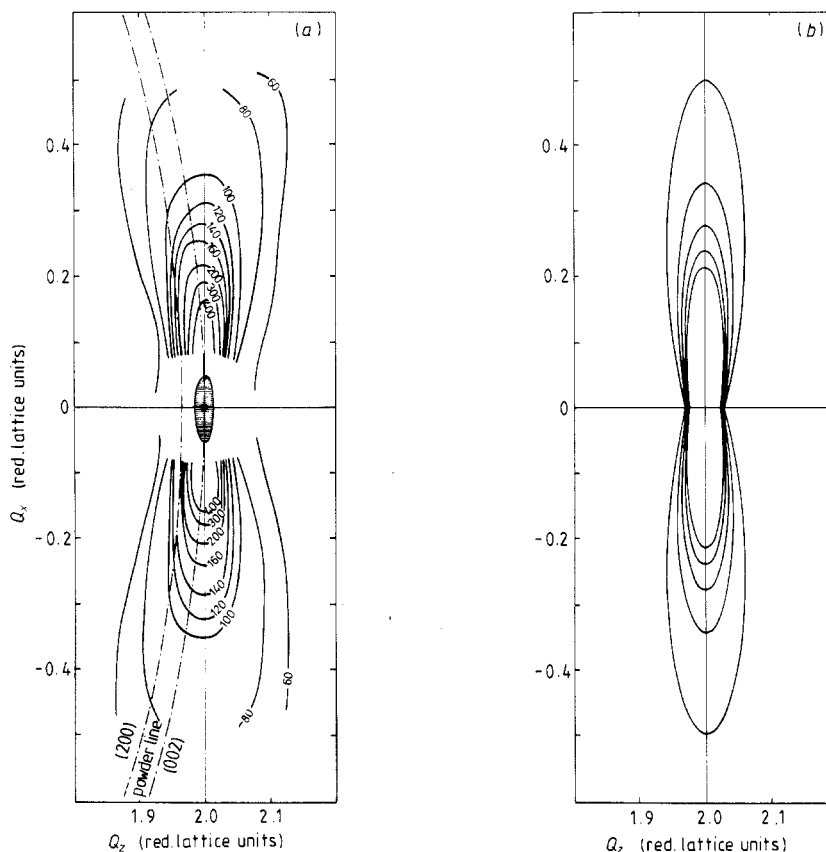
Figure 5. (*a*) Diffuse scattering around (002) measured at $T = T_c + 5$ K on sample A. The background level is about 40 counts min^{-1}. The instrumental resolution is indicated by the shaded ellipse centred at the Bragg point. The data are contaminated with powder lines indicated by the chain curves. (*b*) Calculated iso-intensity contours around (002) at $T = T_c + 5$ K convoluted with the instrumental resolution for sample A. The lines represent equidistant intensity values in arbitrary units. Note the deviations from Huang-type scattering at small q-values due to inelastic contributions. For details of the calculation see text (§ 4.2). Horizontal collimations, 20′–20′–20′–20′; 14.7E_f; $E = 0$ meV.

is reduced. That the linewidths do not vary much in the temperature region investigated is demonstrated by the open circles in figure 6, which denote 2Γ values for $T = T_c + 53$ K.

2.3. Inelastic measurements

The elastic constants of CsCuCl₃ listed in table 1 have been determined by Soboleva *et al* (1976) at room temperature. As a function of T, they were studied by Lüthi (1977), whose measurements on c_{44} are reproduced in figure 7 as full curves. He found that c_{44} is anomalously small in the high-temperature phase and exhibits a large jump at T_c, indicating an acoustic instability. In view of the low-temperature structure one could suspect that the corresponding [001] shear mode will show a softening also at $q = 2\pi/3c$, when approaching T_c from above.

We have, therefore, investigated the transverse acoustic phonon mode propagating along c^* at points $(-2,0,1 + q)$ of the reciprocal lattice by performing constant-Q scans
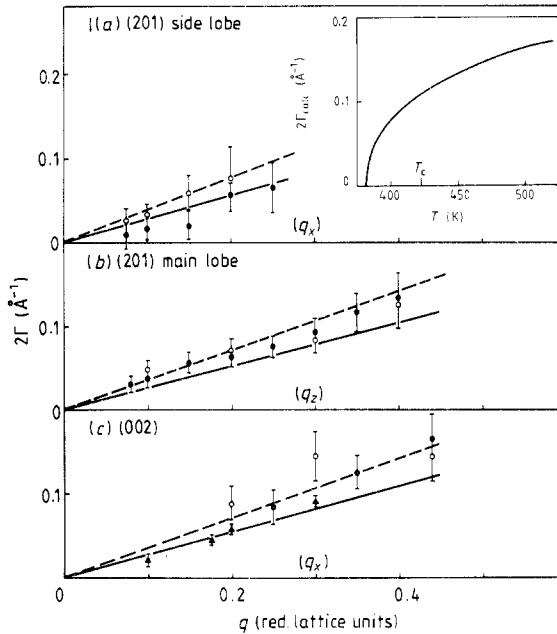
Figure 6. Linewidths 2Γ of quasi-elastic scans performed perpendicular to the long axes of the diffuse intensity lobes around (201) (side lobe and main lobe) and around (002) as a function of q. Full and open circles refer to measurements on sample A at $T_c + 5$ K and $T_c + 53$ K, respectively. The full triangles denote measurements on sample B at $T_c + 5$ K. The linewidths are resolution-corrected, assuming a Lorentzian as intrinsic lineshape for the quasi-elastic scattering. The full and broken lines are theoretical predictions for $T_c + 5$ K and $T_c + 53$ K, respectively. The inset shows 2Γ values calculated for the (201) side lobe at $q_x = 0.40$ as a function of T. Horizontal collimations, $20'-20'-20'-20'$; $14.7E_f$; $E = 0$ meV.

above and below T_c. The open and full triangles in figure 8 denote the positions of the phonon peaks derived from these measurements. It is clear that there is no softening at $q = 0.34$ Å^{-1}, which corresponds to the q-value $2\pi/3c$ where a superlattice Bragg point appears below T_c. A strong overdamping of the phonon signals, however, is observed for $q_z \rightarrow 0$ above T_c, which made it impossible to derive peak positions from phonon measurements at $q_z < 0.15$ in the high-temperature phase.

This phenomenon is connected with the observed anomaly in the elastic constant c_{44}. In the hexagonal system the transverse acoustic phonons propagating along a^* with polarisation parallel to c^* are also determined by c_{44}. For instrumental reasons this branch was more easily accessible in the present experiments and, therefore, the detailed measurements of the acoustic instability were made at points $(q,0,2)$ of the reciprocal lattice. The open and full circles in figure 8 represent the positions of the phonon peaks derived from constant-Q scans below and above T_c. The full and broken curves are sine curves fitted to the peak positions. The small-q measurements below T_c were made by a high-resolution spectrometer set-up with the final neutron energy fixed at 3 meV.

Above T_c, peak positions for phonons with small q-vectors could again not be derived from direct inspection of the measured profiles. While the phonon peaks below T_c are clearly separated from the incoherent peak down to q-values of about 0.04, where the Bragg tails become noticeable, the phonon signals above T_c start to coalesce with a zero-
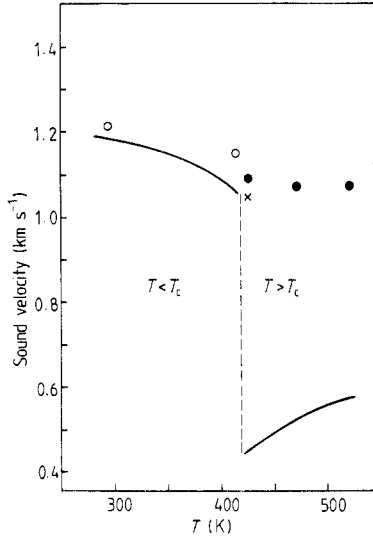
Figure 7. Comparison of sound velocities determined for the c_{44} mode by ultrasonic measurements (full curves; Lüthi 1977) and by inelastic neutron measurements (open and full circles and cross; present work) as a function of T. The neutron values below T_c (open circles) are derived from fits to phonon peak positions, the values above T_c (full circles) from fits of the pseudo-spin model to inelastic measurements. The cross denotes the value derived from a fit to the peak positions of phonons measured at $T = T_c + 5$ K (see broken curve in figure 8).

energy peak at $q \leqslant 0.15$. Figure 9 shows an example for $q = 0.10$, measured just above (full circles) and just below T_c (open circles). For larger q-values, as shown in figure 10, resolved phonon peaks are visible in the measurements above T_c. These peaks, however, are shifted, a large zero-energy peak appears, whose width is broader than the instrumental resolution, and the intensity between phonon and zero-energy peak stays far above the background level, as compared with the corresponding measurement below T_c.

These findings indicate that the large intensity at zero energy, which forms the Huang-type patterns discussed above, may not be interpreted as purely elastic diffuse scattering from a statically disordered array of distorted CuCl$_6$ octahedra; instead, they point to a coupling between phonons and dynamic reorientation processes. Similar phenomena had been observed by Noda *et al* (1980) and were described using the theory of a pseudo-spin–phonon coupled system, which had been developed by Yamada *et al* (1974). We have extended this theory and applied it to the present system. The full curves in figures 9 and 10 are calculated curves, which fit the data very well. An outline of the theoretical approach is given in § 3.

3. Theoretical background

A model for the cooperative Jahn–Teller system in hexagonal perovskites AMCl$_3$ with Jahn–Teller active M^{2+} ions (M^{2+} = Cu^{2+}, Cr^{2+}) has been developed by Schotte (1987). In this approach, elongated MCl$_6$ octahedra are represented by elastic dipoles, which are randomly distributed over six possible orientations. It was shown that it is not

necessary to distinguish between Q_2- and Q_3-type distortions. They both lead to the same result.

The theory has now been refined and extended to include dynamic reorientation processes occurring in such systems. Though it does not give an explanation for the particular mechanism of the first-order phase transition in $CsCuCl_3$, it allows predictions about possible low-temperature structures in the hexagonal perovskites and describes both the quasi-elastic and inelastic neutron measurements in the high-temperature phase of $CsCuCl_3$, in a very satisfactory and coherent way. In detail, the formalism and its application are discussed by Schotte et al (1989). Here, we present a general outline only and the main results necessary for analysing the measurements on $CsCuCl_3$.

The theoretical treatment starts by replacing the Jahn–Teller distorted MCl_6 octahedra with elastic dipoles localised at the positions of the M^{2+} ions. The dipoles are organised in two sublattices according to the two lattice sites of M in the high-temperature unit cell: M(1) at (0,0,0) and M(2) at $(0,0,\frac{1}{2})$ (see figure 1). As shown by Schotte (1987) the dipoles are described by the tensors P^r:

$$P^r = -V_D(\Delta d/d)\left[c_{66}\begin{pmatrix} \hat{P}^r_{xx} & \hat{P}^r_{xy} & 0 \\ \hat{P}^r_{xy} & \hat{P}^r_{yy} & 0 \\ 0 & 0 & 0 \end{pmatrix} + c_{44}\begin{pmatrix} 0 & 0 & \hat{P}^r_{xz} \\ 0 & 0 & \hat{P}^r_{yz} \\ \hat{P}^r_{xz} & \hat{P}^r_{yz} & 0 \end{pmatrix} \right] \tag{1}$$

with

$$\hat{P}^1 = \begin{pmatrix} 1 & 0 & \sqrt{2} \\ 0 & -1 & 0 \\ \sqrt{2} & 0 & 0 \end{pmatrix} \qquad \hat{P}^2 = \frac{1}{2}\begin{pmatrix} -1 & -\sqrt{3} & -\sqrt{2} \\ -\sqrt{3} & 1 & \sqrt{6} \\ -\sqrt{2} & \sqrt{6} & 0 \end{pmatrix}$$

$$\hat{P}^3 = \frac{1}{2}\begin{pmatrix} -1 & \sqrt{3} & -\sqrt{2} \\ \sqrt{3} & 1 & -\sqrt{6} \\ -\sqrt{2} & -\sqrt{6} & 0 \end{pmatrix} \qquad \hat{P}^4 = \begin{pmatrix} 1 & 0 & -\sqrt{2} \\ 0 & -1 & 0 \\ -\sqrt{2} & 0 & 0 \end{pmatrix} \tag{2}$$

$$\hat{P}^5 = \frac{1}{2}\begin{pmatrix} -1 & -\sqrt{3} & \sqrt{2} \\ -\sqrt{3} & 1 & -\sqrt{6} \\ \sqrt{2} & -\sqrt{6} & 0 \end{pmatrix} \qquad \hat{P}^6 = \frac{1}{2}\begin{pmatrix} -1 & \sqrt{3} & \sqrt{2} \\ \sqrt{3} & 1 & \sqrt{6} \\ \sqrt{2} & \sqrt{6} & 0 \end{pmatrix}.$$

Here $r = 1, 2, 3$ refers to the first and $r = 4, 5, 6$ to the second sublattice. The tensors $\hat{P}^r$ of equation (2) describe six crystallographically possible orientations of the dipoles. The actual distortions of the Jahn–Teller units are taken into account by the prefactor $V_D\Delta d/d$ in equation (1). V_D is an effective volume of the elastic dipole and $\Delta d/d$ refers to an elongation, with Δd being the difference between the long and the short axis and d the average axis length of an octahedron. The equilibrium between the Jahn–Teller distortion and the elastic medium is expressed by the product of $V_D\Delta d/d$ and the elastic constants. This product has the dimension of an energy and can be interpreted as an approximate expression for the Jahn–Teller energy:

$$E_{JT} \simeq c_{44}V_D\Delta d/d \simeq \sqrt{2}c_{66}V_D\Delta d/2d. \tag{3}$$

Conceiving the elastic dipoles as pseudo-spins is the important step for incorporating the dynamical properties of the system into the theoretical framework discussed so far. It is achieved by introducing the local concentration $c^r(R)$, which is 1 if a particular
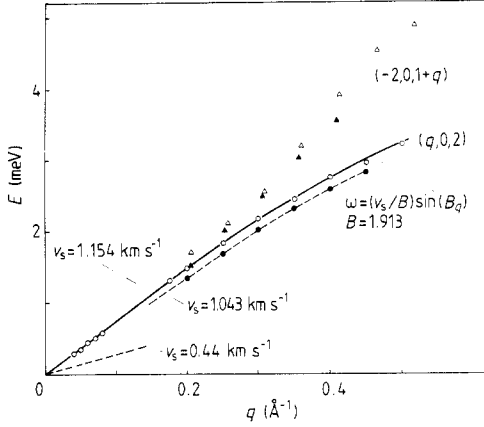
Figure 8. Dispersion curves for TA phonons (c_{44} mode) measured on sample A at $(-2,0,1 + q)$ (triangles) and $(q,0,2)$ (circles). The full and open symbols represent phonon peak positions derived from measurements 5 K above and 5 K below T_c, respectively. Note that in the case of the $(-2,0,1 + q)$ phonons a superlattice Bragg point occurs below T_c at $q = 0.34$ Å^{-1} ($= 2\pi/3c$). The broken and full curves through the full and open circles, respectively, are sine curves fitted to the peak positions of the $(q,0,2)$ phonons. They were used for determining the sound-velocity values shown. For comparison, the dispersion curve corresponding to Lüthi's (1977) c_{44} sound-velocity value $v_s = 0.44$ km s^{-1} at $T = T_c + 5$ K is also indicated by a broken line.
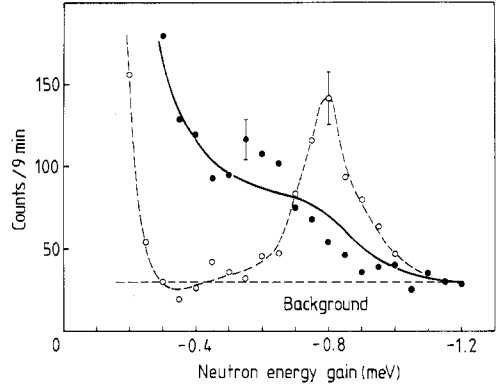
Figure 9. Inelastic measurements 5 K above and 130 K below T_c (full and open circles) performed on sample A at $Q = (-0.10,0,2)$. The symbols represent the raw data. The broken curve through the open circles is a guide to the eye; the full curve is a calculated curve based on the pseudo-spin model and convoluted with the experimental resolution. The background added to the calculated curve is indicated by the broken line. Horizontal collimations, 60′–40′–60′–40′–40′; 5.0E_f.

orientation r is present at site R, and 0 if not. Since there are three possible spin orientations on each site, the system is represented by a three-state Potts model on two sublattices. In second order to the distortions and the pseudo-spins, the elastic energy of such a system can be expressed as

$$E = \tfrac{1}{2}\sum_{RR'} \sum_{rs} J^{rs}(R - R')[c^r(R) - c][c^s(R') - c]$$

$$+ \tfrac{1}{2}\sum_{RR'} D_{\mu\nu}(R - R')u_\nu^*(R)u_\mu(R')$$

$$+ \sum_{RR'} \sum_r G^r(R - R')u(R)[c^r(R) - c] \qquad (4)$$

where $s, r = 1, \ldots, 6$. In equation (4) the first term describes the spin–spin interaction characterised by an exchange parameter J^{rs}, the second term the elastic deformations with **D** being the tensor of the elastic moduli, and the third term the interaction between the spins and the elastic deformations characterised by G^r. The pseudo-spin components are the concentration fluctuations $[c^r(R) - c]$, with $c = \tfrac{1}{3}$ being the mean concentration for a spin of particular orientation at site R. Expanding the displacements $u(R)$ in acoustic normal modes

$$u(R) = [1/(Nm)^{1/2}] \sum_q \sum_{j=1,2,3} [Q_j(q)e_j(q) \, e^{iq\cdot R} + cc] \qquad (5)$$

with m being the mean reduced mass of an atom in the unit cell, and using the eigenvalue equation for the lattice dynamical matrix
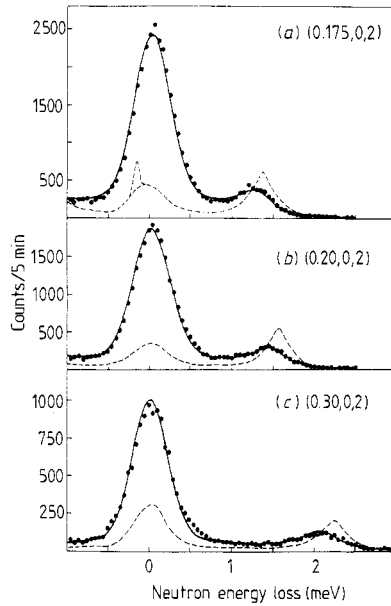
Figure 10. Inelastic measurements 5 K above and 5 K below T_c (full circles and broken curves, respectively) performed on sample B at constant $Q = (q_x,0,2)$ with $q_x = 0.175, 0.20$ and 0.30. The symbols and the broken curves represent raw data; the full curves are calculated curves based on the pseudo-spin model and convoluted with the experimental resolution. The small extra peak in the low-temperature measurement of (a) close to $E = 0$ stems from a weak (002) powder line and demonstrates the rapid degradation of the sample. This low-temperature measurement was made after cycling back from the high-temperature phase. Horizontal collimations, 20'–20'–20'–20'; $14.7E_f$; constant Q.

$$\sum_{R'} D_{\nu\mu}(R - R')e_j^{\mu}(q)\, e^{iq\cdot R'} = m\omega_j^2(q)e_j^{\nu}(q)\, e^{iq\cdot R} \tag{6}$$

equation (4) is transformed into q-space:

$$E = \tfrac{1}{2}\sum_q \sum_{r,s} J^{rs}(q)c^r(q)c^s(-q) + \tfrac{1}{2}\sum_q \sum_j \omega_j^2(q)Q_j(q)Q_j(-q)$$

$$+ \sum_q \sum_j \sum_r Q_j(q)c^r(-q)i(P^r q \cdot e_j)/\sqrt{m}. \tag{7}$$

The derivation of the term

$$i(P^r q \cdot e_j)/\sqrt{m} \equiv h_j^r(q) \tag{8}$$

in equation (7), which describes the pseudo-spin–phonon interaction, is based on the fact that an elastic dipole P_{ij} contributes an elastic energy proportional to the distortion (Khatchaturian 1965, 1966):

$$\delta E \sim P_{ij}\varepsilon_{ij} \tag{9}$$

where the deformations ε_{ij} are defined by

$$\varepsilon_{ij} = \tfrac{1}{2}[\partial u_i(R)/\partial x_j + \partial u_j(R)/\partial x_i]. \tag{10}$$

From the theory of the Potts model an expression for the entropy S (to second order in

$c^r(q)$) of the spin system can be gained, which—combined with equation (7) and extended by a kinetic energy term—gives an expression for the free energy F of the system:

$$F = \tfrac{1}{2}\sum_{q,j} p_j(q)p_j(-q) + \tfrac{1}{2}\sum_{q,j} \omega_j^2 Q_j(q)Q_j(-q) + \sum_{q,j,r} h_j^r(q)Q_j(q)c^r(-q)$$

$$+ \tfrac{1}{2}\sum_{q,r} (J^{rr} + 6kT)c^r(q)c^r(-q) + \tfrac{1}{2}\sum_{q,r} J^{rr+3}c^r(q)c^{r+3}(-q) \tag{11}$$

with $h_j^r(q) = i(P^r q \cdot e_j)/\sqrt{m}$ and $p_j(q)$ the canonical momenta.

Based on this free-energy equation, the correlation function as the time-correlated thermodynamic fluctuations of the elastic deformations (here expressed by phonon amplitudes) has been calculated, using and extending the method of Yamada *et al* (1974). Its Fourier transform enters into the expression for the inelastic neutron scattering cross section. This is a classical method valid for high temperatures, the important steps of which are treated by Landau and Lifshitz (1965). The basic approximation is a relaxational *ansatz* for the equation of motion of the spin

$$c^r(q) \sim \exp(-\gamma t) \tag{12}$$

where $1/\gamma$ is supposed to represent the time a particular spin stays in one of its states r. The spin flips are thought of as being caused by thermal activation involving energies of optical phonons.

Since changes in the d orbitals of Jahn–Teller active ions are not directly probed by neutrons, spin–spin and spin–phonon correlations cannot be detected in the scattering experiment. We give here, therefore, only the result derived for the phonon–phonon correlation:

$$\langle Q_i Q_j \rangle_\omega = (kT/\pi)(h_i(q)h_j(-q)/\gamma\bar{T}^2)\Big\{(\omega^2 - \omega_i^2)(\omega^2 - \omega_j^2)$$

$$\times \Big[\Big(1 + \sum_l^3 |h_l(q)|^2/\bar{T}(\omega^2 - \omega_l^2)\Big)^2 + \omega^2/(\gamma\bar{T})^2\Big]\Big\}^{-1} \tag{13}$$

with $\bar{T} = 6kT$ and

$$h_l = \sum_r h_l^r.$$

The neutron scattering cross section is related to equation (13) in the usual way:

$$\mathrm{d}^2\sigma/\mathrm{d}\omega\,\mathrm{d}q = |\bar{b}|^2 \sum_{i,j} (1/m)(Q \cdot e_i)(Q \cdot e_j)\langle Q_i Q_j \rangle_\omega. \tag{14}$$

Here $Q = H + q$ is the scattering vector with H denoting the Bragg point, while $\bar{b}$ represents the mean scattering power and is basically a scale factor in the present formalism, but will contain the structure factor and the Debye–Waller factor in the fully elaborated theory. Combining equations (13) and (14) the final result can be written as

$$\frac{\mathrm{d}^2\sigma}{\mathrm{d}q\,\mathrm{d}\omega} = |\bar{b}|^2 \frac{1}{\pi\gamma 6kT}\tfrac{1}{6}\sum_r\Big|\sum_i \frac{(Q \cdot e_i)(P^r q \cdot e_i)}{m(\omega^2 - \omega_i^2)}\Big|^2$$

$$\times \Big[\Big(1 + \sum_r\sum_j \frac{P^r q \cdot e_j^2}{m6kT(\omega^2 - \omega_j^2)}\Big)^2 + \frac{\omega^2}{(\gamma 6kT)^2}\Big]^{-1}. \tag{15}$$

4. Results and discussion

Equation (15) is the common basis for analysing both the quasi-elastic diffuse scattering and the phonon measurements. For $\omega = 0$ the double summation term in front of the square brackets becomes equivalent to the Huang scattering formula derived by Schotte (1987), while the term $[\ldots]^{-1}$ is essentially reduced to a susceptibility $\chi(T)$, which determines the temperature dependence of the quasi-elastic scattering together with the prefactor $1/\gamma\bar{T}$. Note that, in the limit $\omega \to 0$, one can replace for any vectors a, b

$$\sum_j \frac{(a \cdot e_j)(e_j \cdot b)}{m\omega_j^2} = \frac{\rho}{m}(a \cdot \mathbf{D}^{-1} \cdot b) \tag{16}$$

where $\mathbf{D}^{-1}$ is the inverse elastic matrix, the components of which are given by Schotte (1987) for the hexagonal system, and ρ is the density of the crystal.

The general form of equation (15) is similar to the expression for a pseudo-spin–phonon coupled system derived by Yamada *et al* (1974). This can easily be seen by comparing their equation (19) with our correlation function (equation (13)) for one normal mode, e.g. $\langle Q_1 Q_1 \rangle$, after rewriting both equations in the following form: equation (19) from Yamada *et al* (1974) becomes

$$\langle QQ \rangle = [(\omega_0^2 - \alpha\omega_0^2)/\gamma_q]/[(\omega^2 - \alpha\omega_0^2) + \omega^2(\omega^2 - \omega_0^2)/\gamma_q] \tag{17}$$

whereas equation (13) from the present work becomes

$$\langle Q_1 Q_1 \rangle_\omega = (kT/\pi)(h_1^2/\gamma\bar{T})/\{[\omega^2 - \omega_1^2 + \Sigma(\omega)]^2$$
$$+ [\omega^2(\omega^2 - \omega_1^2)^2/(\gamma\bar{T})^2\} \tag{18}$$

with

$$\Sigma(\omega) = \frac{h_1^2}{\bar{T}} + \frac{h_2^2}{\bar{T}}\frac{(\omega^2 - \omega_1^2)}{(\omega^2 - \omega_2^2)} + \frac{h_3^2}{\bar{T}}\frac{(\omega^2 - \omega_1^2)}{(\omega^2 - \omega_3^2)}. \tag{19}$$

In equation (17) $\alpha \equiv 1 - g^2(q)/J'(q)$ (for the meaning of these parameters see Yamada *et al* (1974)) can be regarded as a renormalisation parameter, which gives rise to the phonon 'softening' at q-values where the undisturbed phonon frequency ω_0 becomes comparable to the pseudo-spin relaxation rate γ_q. In the present model $\gamma\bar{T}$ has also the meaning of a relaxation rate, while the renormalisation of the phonon frequency is described by the more complicated expression, equation (19). This expression includes contributions from all acoustic modes. The coupling to all acoustic modes results from the interaction of the pseudo-spins through the elastic medium into which they are embedded. Any reorientation of an elastic dipole, i.e. a thermally activated spin flip, produces a strain field, which propagates through the crystal. It is this relaxation process which is sensed by the neutrons and which depends on the properties of the elastic medium as described by the elastic constants of the undisturbed lattice. It will not be possible to observe these constants directly, since the lattice of the high-temperature phase is at any moment locally distorted, but they can be derived from a fit of equation (15) to the quasi-elastic and inelastic measurements. As a first approximation one can assume that they are not too different from the values of the low-temperature phase.

Before comparing with the experiment, the theoretical curves must be convoluted with the instrumental resolution. For this purpose the cross-section function, equation (15), was incorporated in a Cooper–Nathans type resolution program, which itself was embedded in a general least-squares fitting routine. The convolution is performed by

numerical integration, which requires the evaluation of the cross-section function at about 3500 mesh points in the four-dimensional (Q, ω) space.

4.1. Analysis of inelastic measurements

The phonon measurements in the $(h0l)$ zone with $Q = (q_x,0,2)$ are described by the correlation function $\langle Q_1 Q_1 \rangle$. In this high-symmetry direction it is predominantly the behaviour of c_{44} which is observed, and the frequencies ω_i and interaction terms h_i are reduced to the following expressions:

$$\omega_1^2 = q_x^2 c_{44}/\rho \qquad e_1 = (0, 0, 1) \tag{20a}$$

$$\omega_2^2 = q_x^2 c_{66}/\rho \qquad e_2 = (0, 1, 0) \tag{20b}$$

$$\omega_3^2 = q_x^2 c_{11}/\rho \qquad e_3 = (1, 0, 0) \tag{20c}$$

$$h_1^2(q_x)/\bar{T} = A_{\mathrm{JT}} q_x^2 c_{44}^2 = A_{\mathrm{JT}} \omega_1^2 c_{44} \tag{21a}$$

$$h_2^2(q_x)/\bar{T} = A_{\mathrm{JT}} q_x^2 c_{66}^2/2 = A_{\mathrm{JT}} \omega_2^2 c_{66}/2 \tag{21b}$$

$$h_3^2(q_x)/\bar{T} = A_{\mathrm{JT}} q_x^2 c_{66}^2/2 = A_{\mathrm{JT}} \omega_3^2 c_{66}^2/(2c_{11}) \tag{21c}$$

with

$$A_{\mathrm{JT}} = (\rho/mkT)[(\Delta d/d)V_{\mathrm{D}}]^2. \tag{22}$$

For fitting the experimental data the cross-section function (15) was parametrised in such a way that the product $\gamma\bar{T}$, the factor A_{JT} in equations (21) and the elastic constants c_{11}, c_{66} and c_{44} were free variables. A_{JT}, which basically describes the 'dipole strength', is inversely dependent on temperature (see equation (22); for the term $(\Delta d/d)V_{\mathrm{D}}$ see equations (1) and (3)).

All data from constant-Q scans performed at the same temperature were fitted jointly. Thus, the data set for $T_c + 5$ K comprised 540 points with q extending almost over the whole Brillouin zone, from $q_x = 0.04$ to $q_x = 0.45$. In order to allow for a deviation from the linear dispersion relation at higher q-values, equations (20a–c) were modified by replacing q_x by $\sin(Bq_x)$, where $B = 1.913$ had been obtained from a fit to the c_{44} dispersion curve measured at $T = T_c - 5$ K. This procedure should be adequate for describing the unperturbed frequency ω_1 above T_c, as well as below T_c, as shown by figure 8, but is somewhat arbitrary in the case of ω_2 and ω_3.

The only correction applied to the experimental data was the subtraction of a general background, which was supposed to be linear except for the region around $E = 0$, where the incoherent zero-energy peak had to be taken into account. For each curve measured above T_c the appropriate background values were derived from a corresponding measurement below T_c as indicated in figures 9 and 10.

The results of the fits are summarised in table 2. Since the contribution of c_{66} and, especially, c_{11} to the phonon cross section in the measured q direction is small, a refinement of these elastic constants was only tried in the large data set at $T_c + 5$ K. The two parameters are strongly correlated and the error in c_{11} is large. The values obtained, however, are reasonable, when compared with the room-temperature values from sound-velocity measurements.

Lüthi's (1977) ultrasonic measurements and the c_{44} values found in the present work are shown together in figure 7. Our values below T_c, which are derived from a fit to the phonon dispersion (cf. full curve in figure 8), are slightly higher than Lüthi's values. The

Table 2. Results obtained by fitting the pseudo-spin model to inelastic measurements in the high-temperature phase of $CsCuCl_3$. In parentheses are the standard deviations in units of the last digit. The goodness of fit (GOF) and the reliability coefficient (R) are the usual quantities for describing the quality of a fit. They are given by GOF $= \chi^2/(N - p)$ and $R = 100[\chi^2/\Sigma(I_i/\sigma_i)^2]^{1/2}$, with N the number of observations, p the number of parameters, I the observed intensity with error σ and χ^2 the weighted squared deviation.

	$T_c + 5$ K	$T_c + 53$ K	$T_c + 101$ K
c_{11} (10^{10} dyn cm^{-2})	29.1(43)	—	—
c_{66} (10^{10} dyn cm^{-2})	8.23(8)	—	—
c_{44} (10^{10} dyn cm^{-2})	4.32(2)	4.12(2)	4.07(3)
A_{JT} (10^{-10} cm^2 dyn^{-1})	0.093(2)	0.087(1)	0.083(1)
γT (meV)	0.86(2)	1.13(2)	1.26(5)
q_x range	0.04–0.45	0.075–0.50	0.20–0.40
N	540	270	90
R	14.2	15.4	10.2
GOF	2.2	1.5	1.2

value determined from a fit to the apparent phonon peak positions above T_c (broken curve in figure 8), which is marked by a cross in figure 7, lies on Lüthi's low-temperature curve extrapolated to higher temperatures.

In striking contrast to the ultrasonic experiments the sound velocities above T_c, derived from the fitted elastic constants, are rather close to the values below T_c. There is only an 8% change for c_{44}, when T increases from $T_c - 5$ K to $T_c + 5$ K. These fitted elastic constants describe the dynamics of a fictitious, idealised, high-temperature lattice, whereas the ultrasonic measurements see the renormalised sound velocity. In neutron experiments, according to equation (15), separated phonon signals related to the renormalised sound velocity would show up at very small q-values ($q \leqslant 0.03$ Å^{-1}). This q-range could not be resolved in the present experiments.

A_{JT}, as defined by equation (22), should be inversely proportional to T, supposing that the density ρ, the effective dipole volume V_D and the elongation $\Delta d/d$ are only slowly varying with temperature. This is nearly fulfilled by the parameters obtained. The physical quantities, which can be extracted from A_{JT}, like the effective dipole volume V_D or the Jahn–Teller energy E_{JT}, take on reasonable values. Assuming $\Delta d/d = 0.12$ from low-temperature structural data, one arrives at effective dipole volumes for the three temperatures of 28.5, 29.2 and 30.1 Å^3. The slight increase with temperature reflects the increase in V_{cell}. The volumes correspond to spheres of radius $r \simeq 1.9$ Å and, thus, fit well to the size of a $CuCl_6$ octahedron.

The Jahn–Teller energy of a $CuCl_6$ octahedron is supposed to be 1450 cm^{-1} (Reinen and Friebel 1979). According to equation (3) E_{JT} is related to the product of $V_D\Delta d/d$ and the elastic constant c_{44} or c_{66}. With the values derived from the fits one obtains $E_{JT} \simeq 740$ cm^{-1}, using the expression for c_{44}, and $E_{JT} \simeq 1000$ cm^{-1}, using c_{66}. The agreement with the literature value is reasonable, considering the fact that equation (3) represents only an approximation.

The parameter $\gamma\bar{T}$ describes the 'pure' relaxation rate of the pseudo-spins. From the interaction term in the Hamiltonian it contains the product kT and is, therefore, intrinsically temperature dependent. Superimposed is an Arrhenius-type temperature dependence stemming from the thermal activation of the spin flips, from which, too, an increase with temperature is to be expected. The parameters obtained by the fits show the

expected temperature behaviour, though measurements at three different temperatures only are certainly not enough to derive substantiated values for the activation energy. A fit with the function $\gamma_0 T\,e^{-2\beta/T}$ gives 450 K for the activation energy 2β. This is in good agreement with the literature value for the warping term $\beta = 200\ \mathrm{cm}^{-1}$ (Crama 1980), which corresponds to an energy barrier $2\beta = 575$ K between the three possible orientations of the stretched axis in an isolated $CuCl_6$ octahedron.

Relaxation rates derived from the bare $\gamma\bar{T}$ values do not directly correspond to the actual relaxation rates of the pseudo-spins in the lattice. Like the phonons, $\gamma\bar{T}$ is also softened by the 'viscosity' of the elastic medium, into which the spins are embedded. The same softening factor as for the phonons has to be applied. For the actual relaxation rate, therefore, one obtains

$$\Gamma = \gamma\bar{T}\left(1 - \frac{\rho}{6m}\sum_i^6 \frac{(P'^r q \mathbf{D}^{-1} P'^r q)}{kT}\right) \tag{23}$$

which for the $(q_x,0,0)$ direction can be reduced to the following simple form:

$$\Gamma(q_x) = \gamma\bar{T}\{1 - A_{\mathrm{JT}}[\tfrac{1}{2}(c_{66} + c_{66}^2/c_{11}) + c_{44}]\}. \tag{24}$$

Equation (23) is also the expression for the halfwidth Γ at half-maximum of the zero-energy peak at large q, where the phonon signal is separated. Thus, the dynamical properties can be taken directly from the energy width of the quasi-elastic scattering, and from the $\gamma\bar{T}$ values listed in table 2 the following effective relaxation rate can be derived: $\gamma_{\mathrm{eff}} = \Gamma \simeq 0.1\ \mathrm{meV} \simeq 2 \times 10^{10}\ \mathrm{Hz}$.

It should be pointed out that assuming only one well defined relaxation rate in the system is a simplified approach. The goodness of fit, especially for the data at $T = T_c + 5$ K, is somewhat improved when a linear increase of $\gamma\bar{T}$ as a function of q is introduced, which also leads to an increase of the width of the zero-energy peak with q. A direct inspection of the zero-energy peaks also points to a slight increase of the energy width as a function of q, though resolution effects cannot be completely excluded as a possible cause for this observation. Overall, however, the present theory seems to describe the inelastic measurements very satisfactorily, using only two parameters besides the elastic constants, namely A_{JT} and $\gamma\bar{T}$. In A_{JT} it is basically the effective dipole volume V_D that is fitted, and it comes out with a physically reasonable value. The full curves in figures 9 and 10 are calculated curves. The data measured on sample B at the higher q-values are excellently described by the theory (see figure 10), the small-q data measured on sample A are reasonably described (see figure 9). Especially the fits at small q are improved when introducing a q dependence for $\gamma\bar{T}$.

4.2. Analysis of quasi-elastic measurements

Using the results of table 2 and the values of Soboleva *et al* (1976) for c_{33} and c_{13} (see table 1), the quasi-elastic scattering can be calculated by evaluating equation (15) for the nominal energy transfer $\omega = 0$ convoluted with the instrumental resolution. Such calculations for quasi-elastic scans parallel to c^*, however, result in profiles which are sharper than found experimentally. It was concluded that the values of c_{33} and c_{13}, which were determined at room temperature, may not be consistent with the present experiments, and we tried to derive them directly from a fit of equation (15) to the quasi-elastic measurements performed on sample B. Since c_{33} and c_{13} are almost completely correlated in scans parallel to c^*, they could not be refined at the same
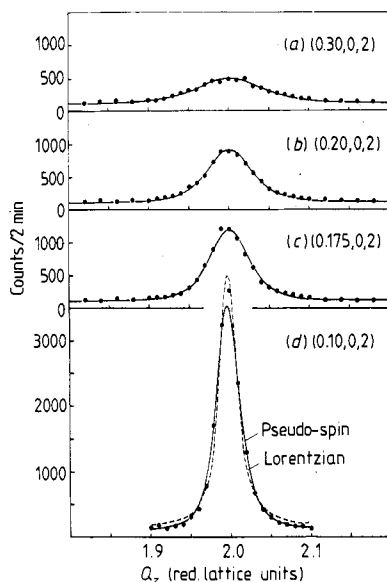
Figure 11. Quasi-elastic scans 5 K above T_c performed on sample B parallel to c^* at distances $q_x = 0.10, 0.175, 0.20$ and 0.30 from the Bragg point (002). The full circles represent the raw data. The full curves are calculated curves based on the pseudo-spin model and convoluted with the experimental resolution. For comparison, a best fit with a Lorentzian is shown as a broken curve in (d). Horizontal collimations, $20'-20'-20'-20'$; $14.7E_f$; $E = 0$ meV.

time. Keeping c_{13} fixed at the reported value, however, and varying c_{33} only, gave excellent fits with $c_{33} = 26.2(4) \times 10^{10}$ dyn cm^{-2}. This value is also in agreement with a preliminary measurement of longitudinal phonons propagating along c^*. The fits to the quasi-elastic scattering are shown in figure 11 as full curves. For comparison, a best fit with a Lorentzian lineshape convoluted with the experimental resolution has also been included in figure 11 (broken curve) for $q_x = 0.10$. The difference between the Lorentzian and the calculated curves shown is small for the higher q_x values, although the tails of the measured profiles are in each case better described by the pseudo-spin model.

Figure 5(b) shows the quasi-elastic scattering around the (002) reflection, calculated by equation (15). The experimental resolution was taken into account. The calculated pattern can thus be compared directly with the measured pattern shown in figure 5(a). The agreement is good, considering the crystal quality of sample A, which makes it difficult to describe the resolution realistically. At small q-values the calculated pattern is clearly different from Huang-type scattering, since more and more phonon contributions are picked up when approaching the Bragg point. Pure Huang scattering has zero intensity along c^* (cf. Schotte *et al* 1989).

When calculating the quasi-elastic scattering around (201) in the same way, it turns out that the shapes of the main lobe and the side lobe, separately, are well reproduced, but not the intensity ratio between them: the main lobe is much shorter in a calculated iso-intensity contour plot than observed. The experimentally found ratio of 1.8 between the lengths of main and side lobes is very close to the value calculated from the Huang term in equation (15) alone (double summation in front of the square brackets). The pure Huang formalism, on the other hand, gives intensity patterns that are broader than those measured.

The discrepancy can be traced back to the particular choice for the orientation of the elastic dipoles expressed by the tensors $\hat{P}^r$ in equation (2), which leads to components $\hat{P}^r_{zz} = 0$ in equation (1). As a consequence c_{33} is not affected by the dipole–dipole interaction and the susceptibility term χ in equation (15) (term in square brackets) for $\omega = 0$ and q parallel to c^* is simply given by

$$\chi(0,0,q_z) = [1 - A_{JT}(T)2c_{44}]^{-1} \tag{25a}$$

while for q parallel to a^*, χ is

$$\chi(q_x,0,0) = \{1 - A_{JT}(T)[\tfrac{1}{2}(c_{66} + c_{66}^2/c_{11}) + c_{44}]\}^{-1}. \tag{25b}$$

Numerically, the terms subtracted from 1 in equations (25) are not much different (0.804 and 0.893, respectively). This small difference, however, gives widely differing factors χ^2 of 26 and 87, respectively, by which the intensities along c^* and a^* are scaled.

At the present state of the theory it is not yet clear whether a refined elastic dipole model including more degrees of freedom would lead to additional terms in equations (25), making $\chi(0,0,q_z)$ equal to $\chi(q_x,0,0)$. Since such an equality is suggested by the experiments, a heuristic correction has been applied to equation (15) for calculating the quasi-elastic scattering around (201) shown in figure 4(b) and the theoretical linewidth values given in figure 6: a scaling factor was introduced in such a way that $\chi(0,0,q_z)$ was forced to become equal to $\chi(q_x,0,0)$ when approaching the c^* axis. By this modification of the theory a satisfactory agreement with the measured (201) main lobe is obtained, while the effects on the (201) side lobe and any scattering concentrated along a^* (e.g. quasi-elastic scattering around (002) and inelastic scattering with $Q = (q_x,0,2)$) are negligible.

The temperature dependence of the quasi-elastic scattering is given by equation (15) as

$$I_{(\omega = 0)} \propto T \exp(2\beta/T)/(T - \theta)^2 \tag{26}$$

where the exponential term stems from the thermal activation of the spin-flip rate $\gamma\bar{T}$. Here θ can be interpreted as T'_c of a second-order phase transition. The temperature-dependent measurements of the quasi-elastic scattering indicate that this phase transition would occur far below the actually observed first-order transition. From equation (25b) T'_c can be calculated to be 382 K. A somewhat lower value is obtained by extrapolating Lüthi's (1977) c_{44} measurement.

For the temperature dependence of the linewidths 2Γ a closed expression cannot be derived from equation (15). As shown in the inset of figure 6(a), 2Γ approaches zero for $T \rightarrow T'_c$. Above 400 K it increases slowly as a function of T and the calculated values could well be approximated by the power law $2\Gamma \propto (T - T'_c)^{1/2.8}$. At each temperature, 2Γ increases linearly with q, as shown by the full and broken lines in figure 6 for $T = T_c + 5$ K and $T = T_c + 53$ K, respectively. This linear increase is characteristic for Huang-type scattering and follows from the $1/q^2$ dependence of the intensity.

5. Concluding remarks

It is a characteristic feature of the quasi-elastic scattering in $CsCuCl_3$ that quantities like the linewidth and the intensity, when expressed as a function of T, point to a

second-order phase transition occurring far below the actually observed T_c, and it is especially the softening of the elastic constant c_{44} that indicates a displacive second-order phase transition. The mechanism that leads to the sudden onset of a first-order order–disorder phase transition at T_c is not explained by the present theory. A third-order term in the free energy of the Potts spin model, which is usually made responsible for a first-order phase transition, has been neglected in the derivation. The experiments suggest that the order–disorder transition is triggered by an evolving displacive transition. Critical fluctuations have not been observed.

The quasi-elastic and inelastic scattering in the high-temperature phase is described very satisfactorily by the present theory, as a function of Q, ω and T. Basically, there is only one parameter, which relies purely on the fit to the experimental data: the spin-relaxation rate $\gamma\bar{T}$. For the other fitting parameters, namely the elastic constants and A_{JT}, at least approximate values can be derived from other measurements. Though the elastic constants, as defined by the theory, could only be observed in the limit of infinite temperature, very good estimates can be gained from systematic measurements of the dispersion relations at high temperature, as was demonstrated for c_{44}. Also A_{JT} is determined by the elastic constants and by the product of an effective dipole volume times the octahedral elongation. For these geometrical quantities reasonable assumptions can be made on the basis of the low-temperature structure. As an additional check, the Jahn–Teller energy can be used, which is also related to A_{JT}, as discussed above.

The spin-relaxation rate $\gamma\bar{T}$ describes the dynamical properties of the high-temperature phase. By measuring the thermal activation of $\gamma\bar{T}$ it is in principle possible to derive the warping energy β for a cooperative Jahn–Teller system, a quantity that is not easily accessible by other methods. This valuable potential of the present theory will be further exploited by studying similar Jahn–Teller systems.

Acknowledgments

References

Crama W J 1980 *Thesis* University of Leiden, The Netherlands
Crama W J and Maaskant W J A 1983 *Physica* B **121** 219
Graf H A, Tanaka H, Dachs H, Pyka N, Schotte U and Shirane G 1986 *Solid State Commun.* **57** 469
Iizumi M, Shirane G and Hirotsu S 1977 unpublished
Khatchaturian A G 1965 *Sov. Phys.–Crystallogr.* **10** 248
—— 1966 *Sov. Phys.–Crystallogr.* **11** 383
Landau L D and Lifshitz E M 1965 *Lehrbuch der Theoretischen Physik* (Berlin: Akademie) vol V, p 415ff and vol VII, p 33
Lüthi 1977 quoted in Hirotsu S J 1977 *J. Phys. C: Solid State Phys.* **10** 967
Noda Y, Youngblood R, Shirane G and Yamada Y 1980 *J. Phys. Soc. Japan* **48** 1576
Reinen D and Friebel C 1979 *Structure and Bonding* vol 37 (Berlin: Springer)

Schotte U 1987 *Z. Phys.* B **66** 91

Schotte U, Graf H A and Dachs H 1989 *J. Phys.: Condens. Matter* **1** 3765

Soboleva L V, Sil'vestrova I M, Perekalina Z B, Gil'varg A B and Martyshev Y N 1976 *Sov. Phys.–Crystallogr.* **21** 660

Tanaka H, Dachs H, Iio K and Nagata K 1986a *J. Phys. C: Solid State Phys.* **19** 4861

—— 1986b *J. Phys. C: Solid State Phys.* **19** 4879

Yamada Y, Takatera H and Huber D L 1974 *J. Phys. Soc. Japan* **36** 641